Preprints (www.preprints.org) | NOT PEER-REVIEWED | Posted: 6 July 2018 doi:10.20944/preprints201807.0107.v1

Peer-reviewed version available at *Sensors* **2018**, *18*, 2781; doi:10.3390/s18092781

Article

An Integrated Wireless, Full-Range, Capacitive Sensor System Designed for Measuring Ventricular Pressure

NH Sebastián[1], DD Alonso[2], FJ Renero-Carrillo[1], Noé Villa-Villaseñor[3] and W Calleja-Arriaga[1*]

[1] CD-MEMS INAOE, Puebla, México; natiely@inaoep.mx, wcalleja@inaoe.mx, paco@inaoep.mx
[2] Center for Engineering and Industrial Development, CIDESI, Queretaro, México; daniela.diaz@cidesi.edu.mx
[3] Advance Technology Center, CIATEQ, San Luis Potosi, México; noe.villa@ciateq.mx
* Correspondence: wcalleja@inaoep.mx

Abstract: This paper reports the novel design of a touch mode capacitive pressure sensor (TMCPS) system with a wireless approach for a full-range continuous monitoring of ventricular pressure. The system consists of two modules: an implantable set and an external reading device. The implantable set, restricted to a 2x2 cm^2 area, consists of a TMCPS array connected with a dual-layer coil, for making a reliable resonant circuit for communication with the external device. The capacitive array is modelled considering the small deflection regime for achieving a dynamic and full 5-300 mmHg pressure range. In this design, the two inductive-coupled modules are calculated considering proper electromagnetic alignment, based on two planar coils and considering the following: 13.56 MHz frequency to avoid tissue damage and three types of biological tissue as core (skin, fat and muscle). The system was validated with the Comsol Multiphysics and CoventorWare softwares; showing a 90% power transmission efficiency at a 3.5 cm distance between coils. The implantable module includes aluminum- and polyimide-based devices, which allows ergonomic, robust, reproducible, and technologically feasible integrated sensors. In addition, the module shows a simplified and low cost design approach based on PolyMEMS INAOE® technology, featured by low-temperature processing.

Keywords: RF MEMS, Pressure Sensor; MEMS Resonators; Implantable BioMEMS; Flexible Electronics, Touch Mode Capacitive Sensor.

1. Introduction

This work addresses a new alternative for measuring blood pressure, using a novel LC sensor arrangement, which can overcome some restrictions that are due to the reduced implantation area available at the left ventricle (LV). Some recent alternatives are still considering the pulmonary artery anatomy dimensions, since it can allow a wider area for the implantation of a more powerful LC radiating inductor [1], however, they are characterized by a limited pressure range [2]. Some biomedical and technology details are described below.

Regarding sensors placed inside the human body for the measurements and wireless transmission of physiological parameters, some cases were proposed since several decades ago. In 1967, C. Collins [3] developed a passive miniature sensor for the continuous measurement of the intraocular pressure on patients with glaucoma. This device was based on a passive LC resonant circuit, in which the resonant frequency was varied according to the embedded pressure surrounding the device. The electromagnetic coupling of the sensor to an external loop allowed for the wireless transmission, hence determining the resonant frequency of the LC sensor. Then, and considering some suitable calibration, that sensor was able to read the embedding pressure. Starting from that work and with the current advances in microelectronics and microelectromechanical systems (MEMS), several groups began conduct research based on the same principle [4-12]. As was evidenced, the available area for the LC array versus power transmission is the main issue to be solved for this kind of implantable sensors, calling for technological improvements in order to meet the implantation requirements.

Blood pressure problems are a kind of disease that chronically damages the blood vessels, organs and tissues of the human body. Public information shows that at least 10% of the world population suffers from these diseases, with the high blood pressure being the main cause of morbidity and mortality in the world [12-15]. In the heart, the contractions of the ventricular chambers, left and right, provide the force to send the blood to the human limbs, however, sometimes the heart cannot provide enough force to send the blood to the whole body [2]. Thus, it is desired to perform some real time pressure measurements directly inside the chambers of the heart. Accordingly, a successful ventricular pressure monitoring is crucial in medical diagnosis on a series of diseases such as heart failure, aortic aneurysms, strokes, arteriosclerosis and renal failure [16,17].

Currently, there are several blood pressure measurement systems; the most common are the non-invasive devices such as air-filled blood-pressure cuffs linked to a sphygmomanometer and the via auscultator sound method [18]. In addition, non-invasive blood pressure measurements lack of accuracy and stability, since they are indirect measurement techniques [17]. On the other hand, current invasive methods are typically used for percutaneous arterial catheter system, which although are very accurate, they inhibit the free movement of the patient and might be unsafe for long-term use due to complications such as trauma to arterial vessels, infection, hemorrhage and difficulty in obtaining access [18-21].

The development of polymeric materials has represented one of the most significant tools for the medical area and bioengineering research, since the use of new materials has allowed significant advantages for obtaining implantable devices that can work for a long time, besides they also present additional advantages, such as biocompatibility, low weight, mechanical flexibility and the use of minimally invasive implantation techniques.

In 2006, Fonseca et al. [22] published the first flexible wireless pressure sensor for monitoring abdominal aortic aneurysms. This device was fabricated using a flexible polymer and ceramics which incorporated using lamination techniques, in order to implement a passive resonant circuit. Although this work represents one of the first academic contributions about implanted blood pressure monitors with strong consideration for biocompatibility and minimally invasive functionality, the device precision showed limitations by signal drift and the distance of the electromagnetic transmission.

In 2006 [11], began the development of a new class of implantable devices for the control of aortic aneurysms and heart failure. The system was named CardioMEMS™ [23-27], and consists of an implantable pressure sensor, an external communication module and an intravenous supply system designed to deploy the sensor in the pulmonary artery. The battery-less 3.5×30 mm device has a wireless range of about 20cm. The micromachined device was fabricated utilizing two fused silica wafers, electrodeposited inductors, and fusion bonding. Once implanted, the CardioMEMS™ sensor provided hemodynamic data for systolic pulmonary pressure of 15-35 mmHg, diastolic pressure of 8-20 mmHg and a mean of 10-25 mmHg [26, 28]. In 2014 this system was approved by FDA and according to the CHAMPION study, the use of this device in patients with heart failure (HF) has allowed for a reduction of hospitalization events which improved the life quality of the patients [28-29].

CardioMEMS™ sensor and most of the pressure sensors designed to be implanted in a place near the heart, are mainly placed in the pulmonary artery (PA), since the pressure in this site can be related to a series of diseases such as heart failure, pulmonary hypertension and aortic aneurysms [19, 23-25]. In addition, the implantation of pressure sensors in the PA offers a series of design and manufacture advantages such as reduced pressure range (0-80 mm Hg), large devices due to the size of the PA (3x3 cm), and the use of techniques for minimally invasive implantation. However, the pressure range measured in PA cannot be related directly to cardiac ventricular contraction and relaxation event. Therefore, if a reliable ventricular pressure sensor can be fabricated and implanted, new diagnostic and therapeutic possibilities could be open, because the LV is the chamber of the heart responsible for pumping the oxygenated blood to the circulatory system [2, 29]. As a result, the

Peer-reviewed version available at *Sensors* **2018**, *18*, 2781; doi:10.3390/s18092781

continuous monitoring of left ventricular pressure, could allow the control of diseases such as: heart failure, hypertrophy in the LV and hypertension; additionally, this will allow the control of secondary diseases such as strokes, renal failure, myocardial infarctions, disease in the coronary artery and aortic aneurysms, placing the sensor permanently in the aneurysmal sac [8, 17,19,20-21,30-43]. Figure 1 shows a geometrical approach for the left ventricle, this section is proposed for the sensor implantation, with an inner available area of 2x2 centimeters [44].

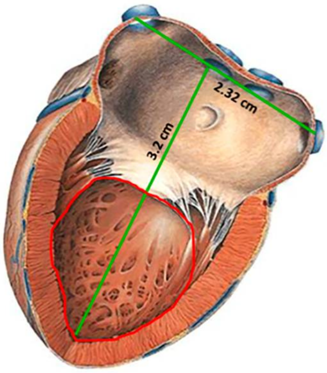

Figure 1. Sketch of the left ventricle [44]; showing the inner section proposed for the sensor implantation.

Therefore, an implantable LV pressure device that meets the following considerations is required: wide range of operating pressure (5 to 300 mmHg), small size, appropriated frequency bandwidth, high resolution and precision, biocompatibility and stability in hostile environments. In addition, the sensor design must take into account minimally invasive techniques and anchoring schemes that prevents displacements of the sensor.

This paper reports the novel design of a two inductive-coupled modules designed for a continuous monitoring of LV pressure. The conception of the implantable capacitive array and the inductive coupling link are designed for accomplish practical, accurate, and real-time wireless pressure sensing. This novel design is supported by our previous work: a) A magnetically coupled planar coils for wireless power transfer in intraocular pressure measurements [45]; b) An aluminum based thin film technique for the fabrication of capacitive sensors [46-47], and c) The implantation of an experimental LC prototype beneath the conjunctiva of a rabbit´s eye using a very simple surgery. The sensors array has the capability to adjust between the conjunctiva and the cornea without an aggressive invasive procedure; the LC array did not suffer rejection; tissue irritation disappears after three weeks; the prototype showed good stability, and the rabbit tolerated this implant during six months before its sacrifice [48]. Figure 2 shows images of this previous work. This implantable sensor is still under fabrication considering a thin-film monolithic approach, defining the capacitive and inductive structures in the same flexible/foldable ergonomic substrate, without the use of hybrid-like connections, combining two manufacturing technologies: surface micromachining and flexible electronics.

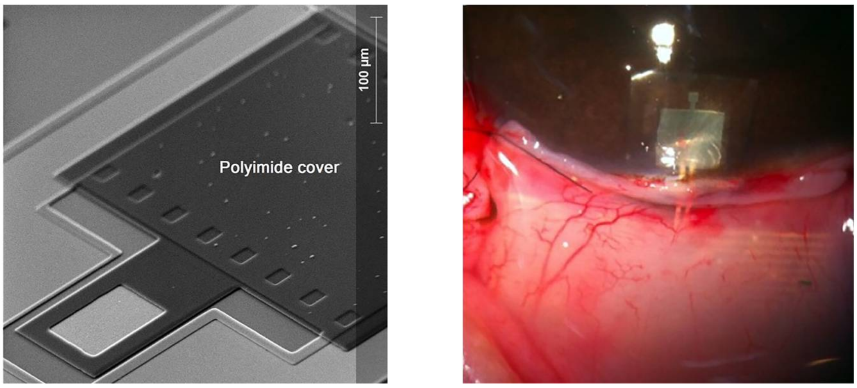

(a) (b)

Figure 2. a) Aluminum based capacitive pressure sensor fabricated over a thick polyimide substrate and capped with a thin polyimide film. b) Flexible LC prototype implanted in the rabbit´s eye [45, 47-48].

The fabrication process was designed according to the PolyMEMS INAOE® technology, which is featured by a low-temperature processing, considering materials for assuring biocompatibility. Finally, this sensor can also be adapted for monitoring the pressure in different organs, such as the aorta, pulmonary artery and even the urinary bladder.

2. Integrated Wireless System Description

The concept supporting the wireless ventricular pressure sensor, in a passive electrical sensing scheme, is shown in Figure 3. The complete monitoring system consists of two modules: an implantable sensor set and an external reader device. In this design, the two inductive-coupled modules are calculated considering a proper electromagnetic alignment, based on two circular planar coils with the proper resonant frequency, calculated as [49-51]:

$$f=\frac{1}{2\pi\sqrt{LC}} \qquad \text{if} \qquad R^2 \gg \frac{L}{C} \tag{1}$$

Where L, C and R denotes the magnitudes for inductance, capacitance and resistance, respectively. In addition, for this design both coupled modules are modelled as a multicore transformer for transmission/reception power. That is, when a time varying current circulates though the coil (L_r) from the reader device, an electromagnetic field is radiated around it. If the coil (L_s) from the implantable set is inside the radiation zone, some electromagnetic field lines cross the L_s area, generating a time varying current on the implantable set and operates according to the C_s magnitude. C_s will vary following the ventricular pressure, and the proper electromagnetic coupling is the main subject for this work.

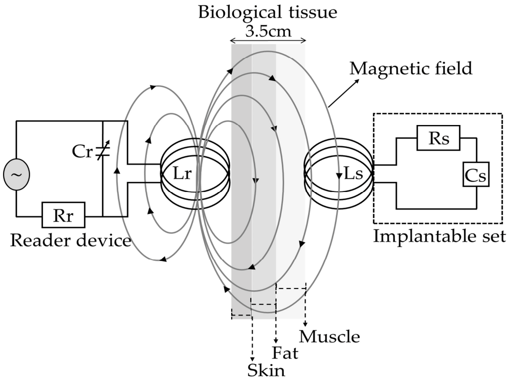

Figure 3. Electromagnetic scheme for the wireless ventricular pressure sensor.

The resonant frequency of the implanted sensor set and the signal coupling towards the external coil can be modeled as a two-port network. Under this premise, the input impedance of the reader coil is expressed taking electrical parameters from the implantable device [49-50, 52], as follows:

$$Z_{eq}=\frac{V_r}{I_r}=j2\pi fL_r\left[1+k^2\frac{(f/f_s)^2}{1-(f/f_s)^2+(1/Q_s)j(f/f_s)}\right] \tag{2}$$

Where V and I are the exciting voltage and current across the reader coil, f is the excitation frequency, k is the coupling factor (totally dependent on physical dimensions), f_s is the resonating

Peer-reviewed version available at *Sensors* **2018**, *18*, 2781; doi:10.3390/s18092781

frequency of the implanted sensor set and $Q=(2\pi f_s L_s)/R_s$ is the quality factor of the sensor under resonance.

It can be seen from Equation 2, that in order to change the impedance Z_{eq} from de reader coil, one must change either the k or f_s of the implanted set. For ventricular pressure applications, the distance between both coils will remain constant so the k will not change. Therefore, f_s is the only parameter capable of changing the equivalent impedance. According to Equation 1, the overall variation of the capacitance into the implanted sensor array is caused by a local change of the pressure, which accordingly changes the resonant frequency. Such changes are detected in the reading coil as variations in the equivalent impedance, and hence related to the ventricular pressure.

2.1 Implantable LC sensor set

The implantable sensor set, restricted to a 2x2 cm^2 area (according to the LV internal dimensions), was defined over a 20 µm-thick polyimide film and interconnected according to Figure 1. It consists of 2 touch-mode capacitive pressure sensor (TMCPS) parallel array connected to a dual-layer planar coil, thus a reliable resonant circuit for communication with the external device is attained. The implantable set has been designed considering a thin-film monolithic approach, underlying the capacitive and inductive structures in the same flexible ergonomic substrate without the use of hybrid-like connections, combining two manufacturing technologies, such as surface micromachining and flexible electronics. Figure 4 shows a 3D view of the double-layer coil and a cross-section view of the implantable sensor set.

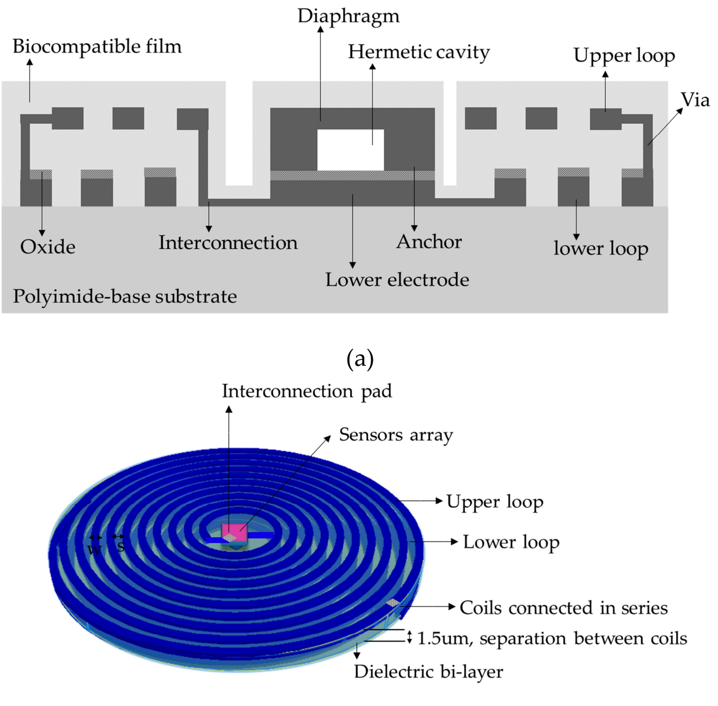

(a)

(b)

Figure 4. a) Cross section cut of the implantable sensor set and b) A 3D view.

The proposed novel capacitive array is shown in Figure 5a, it consists of a sectioned hermetic chamber with 2 parallel capacitors array. In this approach, both plates are isolated by a double insulator: air/silicon oxide, allowing a dynamic variable capacitive sensor [47, 53-55], as can be seen in the layout of Figure 5b. The 555 µm-side capacitor is mechanically designed for response under the lower LV pressure regime and the 300 µm-side capacitor is designed to obtain a response under the higher LV pressure regime. This capacitive array is fully designed considering a thin polyimide film, which is added as a biocompatible capping film, i. e., at the same time is part of the diaphragm of the capacitors. Finally, the capacitors are analyzed as follows: a) the top diaphragm is calculated to provide a direct contact with the physiological environment; thus, the structures are properly covered with a biocompatible film; b) the double-film squared diaphragm (polyimide over aluminum) was structurally modeled considering the small deflection regime [54-55]. This analytical work has concluded with 2 precise mechanical complementary capacitors, capable of achieving a dynamic and full 5 - 300 mmHg pressure range to cover the full diastolic-systolic pressure range developed across the LV [2, 19].

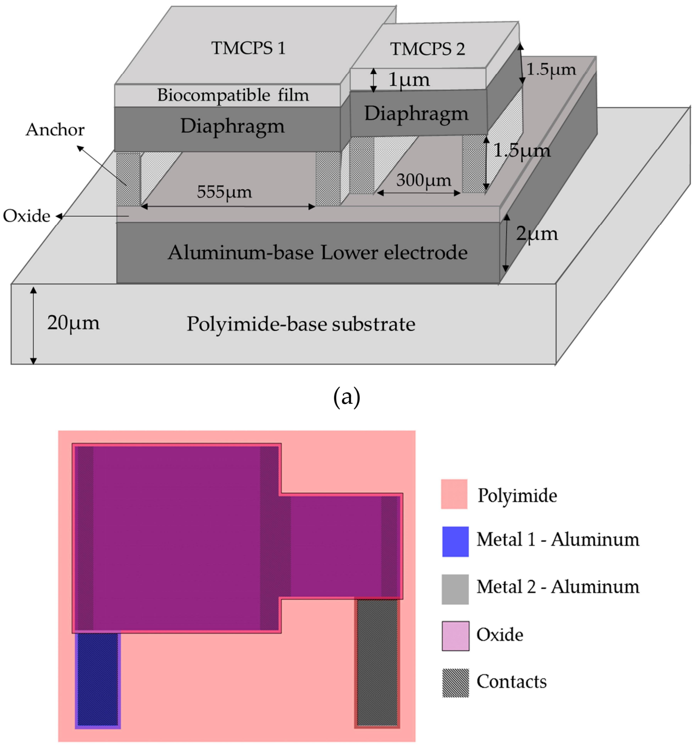

(a)

(b)

Figure 5. a) Double diaphragm capacitive array, the sketch shows structural materials and dimensions. b) Layout.

The detection principle for the capacitive array is based on the relationship between the changes in capacitance under the applied pressure [8, 47, 49, 54]. In this case the total capacitance, at any time, is the sum of the individual capacitances associated at a given pressure, as follows:

$$C_s=\frac{\varepsilon_0\varepsilon_{aire}\varepsilon_{d1}A_{touch1}}{W_{max1}+\varepsilon_{d1}W_{max1}}+\frac{\varepsilon_0\varepsilon_{aire}\varepsilon_{d2}A_{touch2}}{W_{max2}+\varepsilon_{d2}W_{max2}} \qquad (3)$$

Where ε_d is the dielectric constant of the insulating material, A_{Touch} is the contact area of the diaphragm, W_{max} is the separation distance between the parallel metal plates and the subscripts 1 and 2 indicate the first and second capacitive structure, respectively. Table 1 shows the main parametric design and the analytical results for the capacitive array. Both diaphragms were calculated to operate simultaneously based on the minimum and maximum operating pressure of the LV, that is, the first structure operates from the minimum pressure of 5 mmHg and the second one operates up to a maximum pressure of 300 mmHg, thereby ensuring that the capacitive assembly covers the full range for the ventricular pressure.

Table 1. Parameters design and analytical results for the capacitive array.

Parameters	Symbol	Structure 1	Structure 2
Contact pressure	P_{Tocuh}	5 mmHg	40 mmHg
Maximum operating pressure	P_{Max}	200 mmHg	300 mmHg
Lateral length of the diaphragm	a	555 µm	300 µm

Thickness of the lower electrode	t_{Elow}	2 µm	2 µm
Thickness of the top electrode	t_{Etop}	1 µm	1 µm
Thickness of the biocompatible film	t_{Bio}	1.5 µm	1.5 um
Air gap	W_{max}	1.5 µm	1.5 µm
Oxide thickness	t_{oxi}	0.2 µm	0.2 µm
Sensor capacitance at zero pressure	C_{p0}	1.9 pF	0.51 pF

Because the restricted area existing inside the LV, the design of the internal coil consists of a dual-layer planar inductor to increase the total value of the inductance and its quality factor. The two superposed aluminum loops, insolated by a dielectric bi-layer (oxide and polyimide), are connected in series and composed by 28 turns each, covering an external diameter of 2cm. Regarding the metal and coil thickness, they were chosen based on the full implantable set to facilitate the thin-film monolithic approach. As shown in the layout of Figure 6, the full array is covered by a thin polyimide film.

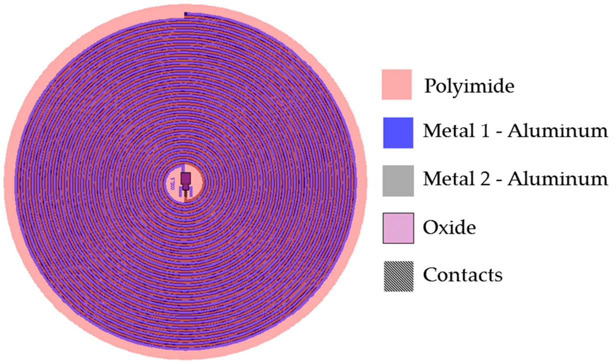

Figure 6. Double layer internal coil, layout showing the 5-level design.

The electrical characteristics of the dual-layer planar coil can be determined by using established models [56-58], where the electrical inductance for a circular multi-layer coil is calculated as:

$$L \cong L_1 + L_2 \pm 2M \tag{4}$$

Where $M=k(L_1 \cdot L_2)^{1/2}$ is the mutual inductance between the two levels of the planar coil [28], $k=(R^2_{out.T} \cdot R^2_{out.R})/(R^2_{out.T} \cdot R^2_{out.R})^{1/2}(R^2_{out.T}+X^2)^{3/2}$ is the coupling factor between two coils, whereas L_1 and L_2 are the self-inductances for the lower and upper loops, which are determined from the following Equation [49-50, 57, 59]:

$$L_1 = L_2 \cong \frac{\mu_0 n^2 d_{avg} C_1}{2}\left[\ln\left(\frac{C_2}{F}\right) + C_3 F + C_4 F^2\right] \tag{5}$$

Where n=(Rout - Rin)(w+s) is the number of turns of the inductor, davg=(Dout+Din)/2 is the averaged diameter of the windings, F=(Dout-Din)/ Dout+Din) is the fill factor of the windings and C1 – C4 are constant coefficients determined by the winding geometry [57].

From Equation 4 we can observe that for a multi-layer system, the final inductance increases according to a positive effective mutual coupling. Figure 6 shows the layout of the sensor set. This design has several advantages that include small size, stability, ergonomic and mechanical flexibility. Additionally, the distribution of the windings are not superposed, in this way there is no contribution to parasitic capacitance and the mutual coupling results positive.

2.2 External Coil

The external coil was calculated under flexible conditions taking into account the physical dimensions and materials for manufacturing; it was projected on a 4-layer PCB FR-4 as the substrate material; composed by 27-turns cooper coil and 8-cm outside diameter, and designed following the Finkenzeller condition, according the following Equations [52, 59]:

$$D_{out.T} \leq D2\sqrt{2} \tag{6}$$

$$R_{out.T} \geq \sqrt{X^2 + R^2_{out.R}} \tag{7}$$

Where $D_{out.T}=2R_{out.T}$ is the outer diameter of the outer coil, D is the radiation distance and X is the separation between the inner and outer coils.

The electromagnetic coupling was calculated considering the following: a) 13.56 MHz frequency to avoid tissue damage by radiation and heating (according to ISO 14117 for implantable devices) and b) in order to simulate a more realistic environment, the core considers three components for the biological tissue: the first layer is skin with 0.5 cm thickness, the second layer is fat with 1 cm thickness and the third layer is muscle with 2cm thickness. Design parameters such as the number of turns, width, thickness and value for the inductive element are determined based on the self-inductance value of the implantable sensor set, so that the two RCL circuits resonate at the same frequency. Figure 7 shows the lay out of the external coil.

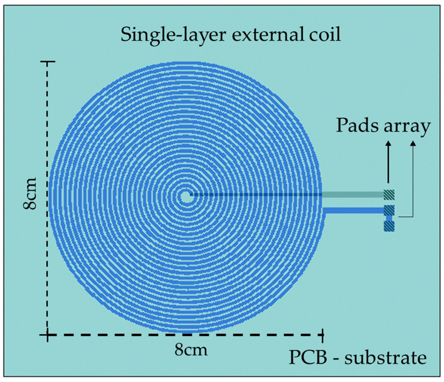

Figure 7. Layout generated **for** the external coil.

The self-inductance of the external coil as well as for the internal coil were calculated based on the number of turns taken from Equation 5. For the inductive coupling link, the electrical parameters were calculated using well known methods [51, 59-60], and then the power transmission efficiency for the inductive link is given by:

$$\eta = \frac{k^2 Q_1 Q_2^3 R_2 R_{load}}{\left(k^2 Q_1 Q_2^3 R_2 R_{load} + k^2 Q_1 Q_2 R^2_{load} + Q_2^4 R_2^2 + 2 Q_2^2 R_2 R_{load} + R^2_{load}\right)} \tag{8}$$

Where $Q=(1/R)(L/C)^{1/2}$ represents the quality factor for the external and internal coils, R_2 is the equivalent resistance of the internal coil, $R_{load} \geq 2\omega L_2$ is the load resistance [59], and for this case $R_{load}=3$ kΩ. Table 2 shows the main parametric design and the analytical results for the internal and external coils.

Table 2. Analytical and design parameters for the internal and external coils.

Quantity	Symbol	Internal coil	External coil
Internal diameter	Din	2 mm	2 mm
External diameter	Dout	2 cm	8 cm
Width of the metal lines	w	160 μm	700 μm
Space between turns	s	160 μm	700 μm

doi:10.20944/preprints201807.0107.v1

Peer-reviewed version available at Sensors 2018, 18, 2781; doi:10.3390/s18092781

Thickness of the metal lines	h	2 µm y 1 µm	35 µm
Number of turns	N	28 each loop	27
Length	l	1.14 m	1.7 m
Frequency of operation	fs	13.56 MHz	
Self-Inductance	L	20.05 µH	21.29 µH
Electrical resistance	R	309 Ω	4 Ω
Quality factor	Q	8	591
Load resistance	Rload	3 kΩ	---
Radiation distance	X	3.5 cm	
Coupling coefficient	k	0.054	
Mutual inductance	M	2.5 µH	
Power transmission efficiency	η	90%	

3. Results and Discussion

3.1. Capacitive array

The capacitive array was analyzed using the CoventorWare® software based on the finite element method to evaluate the mechanical deformation of both diaphragms. In addition, the obtained parameters (strain, stress, electrical resistance, and finally the C-P characteristics) and the resultant quantitative curves were used as a design tool to achieve a desired electromechanical performance. Figure 8a compares both, the analytical and simulated diaphragm maximum deflection P-W_{max} versus the applied pressure, obtained from the designed squared capacitive structures: 555 µm- and 300 µm-side. Figure 8b illustrates the initial touching operation pressure (P_{Touch}) for each diaphragm.

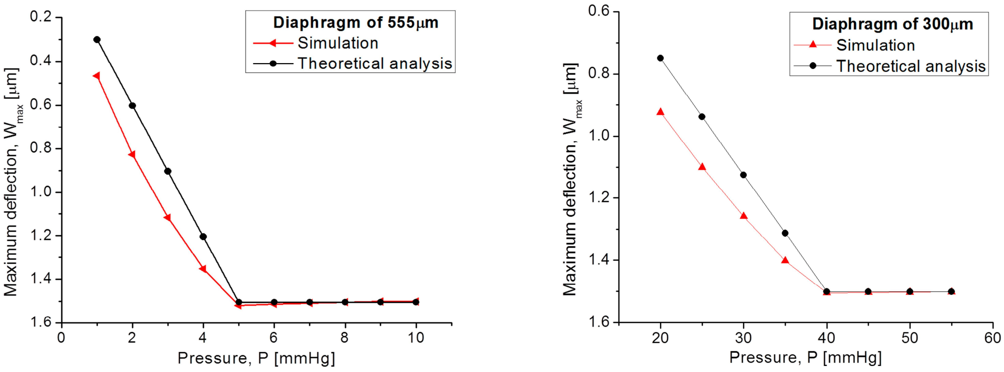

(a) (b)

Figure 8. Comparison of analytical and simulated P-W_{max} curves obtained from (a) 555 µm-side diaphragm and (b) 300 µm-side diaphragm.

Figure 9 allows the 3D qualitative visualization for the mechanical response under an applied pressure. It can be observed that the large structure operates at the low pressure regime and the small one operates at the high pressure regime.

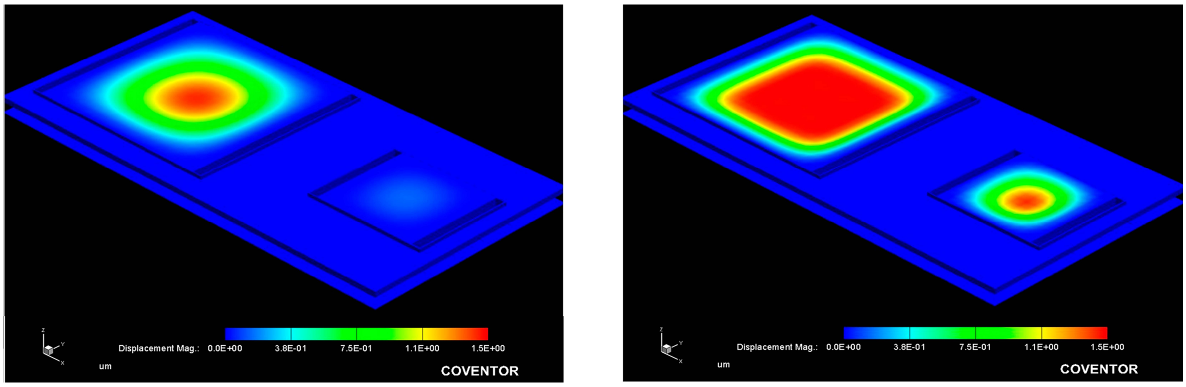

(a) (b)

Figure 9. Simulated mechanical response, obtained from the capacitive array at (a) 10 mmHg and (b) 100 mmHg applied pressure.

From Figure 8, the analytical model agrees well the calculated mechanical response, where the maximum deflection (touching pressure) occurs at 5 mmHg and 40 mmHg, according to the size for each squared diaphragm. The slight variation observed at the beginning of the P-W_{max} curves are due the fact that the analytical calculations neglects some deformations at the middle plane of the composed diaphragm, and the simulation software recreates the complete trajectory of the diaphragm, considering key structural parameters and a more complex analysis.

Once the capacitance (TCMPS) parameters have been determined for achieving an optimum performance, the maximum operating pressure is evaluated according to the increasing pressure over the diaphragms, hence simulating the touching contact area ($A_{contact}$) over the isolated lower plate. Therefore, once the contact area does not increase anymore, the applied pressure at this point is the maximum operating pressure. Figure 10 shows the P-$A_{contact}$ graphs, where the maximum operating pressure for each capacitive structure are plotted. The lower pressure regime corresponds to the 550 µm diaphragm, and the higher pressure regime is for the 300 µm diaphragm.

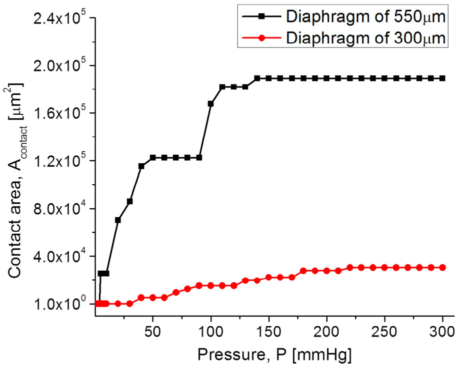

Figure 10. P-$A_{contact}$ graphs for the capacitive (TMCPS) sensor array.

In both diaphragms under increasing pressure regime, the variations of the touching contact area seem slight, however these variations are enough to produce significative changes in the overall capacitance, and consequently produce changes in the resonant frequency of the RCL circuit (see Equation 1). The touch contact area can be expressed as $A_{Touch}=K_1P-K_2P^2$, where K_1 y K_2 are linear and saturation constants, respectively, and $K_1>>K_2$ [53]. Therefore, under a determined pressure, the contact area is proportional to the pressure, and the corresponding capacitance is directly determined. This is because the overall response is a linear C–P relationship, typical of a touch mode capacitive pressure sensor, which is very suitable for conditioning circuits. Figure 11 shows the characteristic C–P curves obtained for each one and the full set of capacitive sensors as well.

Peer-reviewed version available at *Sensors* **2018**, *18*, 2781; doi:10.3390/s18092781

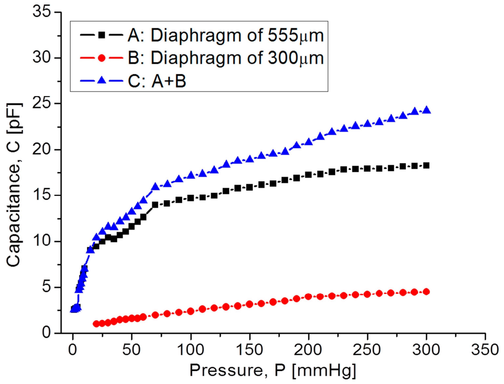

Figure 11. Capacitance response versus applied pressure, covering a full 5-300 mmHg range.

In Figure 11, graph C, it can be seen that at the beginning the capacitance increases suddenly because the 555 µm diaphragm quickly makes contact over the lower electrode. In the 15 – 75 mmHg range, the capacitance increases with a linear rate typical for the 555 µm diaphragm. Around 80 - 300 mmHg, the capacitance increases linearly and steadily, influenced by the 300 µm diaphragm according to the simulation routines. This electromechanical response from the capacitive sensor set is analyzed once it is interconnected with the planar coil. As expected, the capacitance variations lead to changes over the resonant frequency. Figure 12 shows the simulated operating frequency versus the capacitance variations, according to the circuit shown in Figure 3.

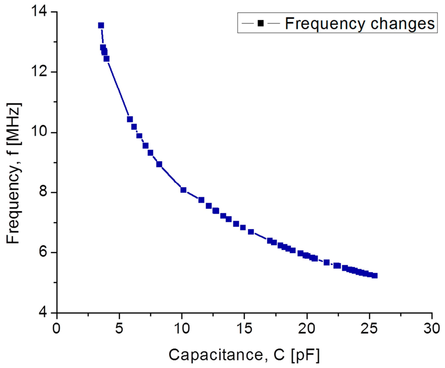

Figure 12. Simulated operating frequency as a function of capacitance for the implantable set.

According to simulations, the operating frequency for the implantable sensor set has a variation from 13.56 MHz to 5.2 MHz, this frequency range which is included within the industrial, medical and scientific band (ISM), and completely ensures the safety because no tissue damage by radiation can occur. Another key parameter for analyzing the capacitive pressure sensor is the sensitivity $\Delta C/\Delta P$ as a function of frequency.

Our mathematical analysis and simulations make evident some changes in the sensor sensitivity, considering the operating frequency range. Figure 13 shows the relationship between the sensitivity and the applied pressure, considering each capacitive structure. As observed, the sensitivity decreases when the applied pressure increases. This sensitivity is influencing the final power transmission efficiency to be discussed later.

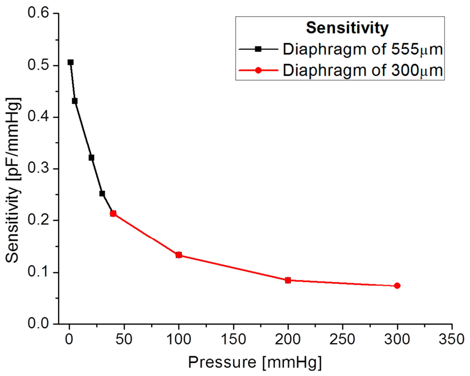

Figure 11. Sensitivity versus applied pressure.

3.2. Inductive coupling link

The overall inductive coupling link was modeled considering three main factors (internal dual-layer coil, external coil and protocol coupling link), using the Comsol Multiphysics® software based on physical interfaces and finite element analysis. Each factor was modeled explicitly and with a homogenized approach for obtaining diverse parameters, such as: self-inductance (L), mutual inductance (M), electrical resistance (R), magnetic flux density (Φ) and induced current (i).

3.2.1. Internal dual-layer coil model

The internal dual-layer coil is simulated by parts and as a single-element, because a multilevel coil involves more coupling factors, than a single-layer coil (see Equation 4). As a composed-element, a self-inductance of 6.68 µH was obtained for each loop, and an electric resistance of 77 Ω and 158 Ω were obtained for the lower and upper loop, respectively. For the single-element coil, separated 1.5 µm by a dielectric material (polyimide) and planarly oriented, a coupling factor of 0.99, a self-inductance of 27.1 µH and an electrical resistance of 259 Ω were obtained, this is shown in Figure 14.

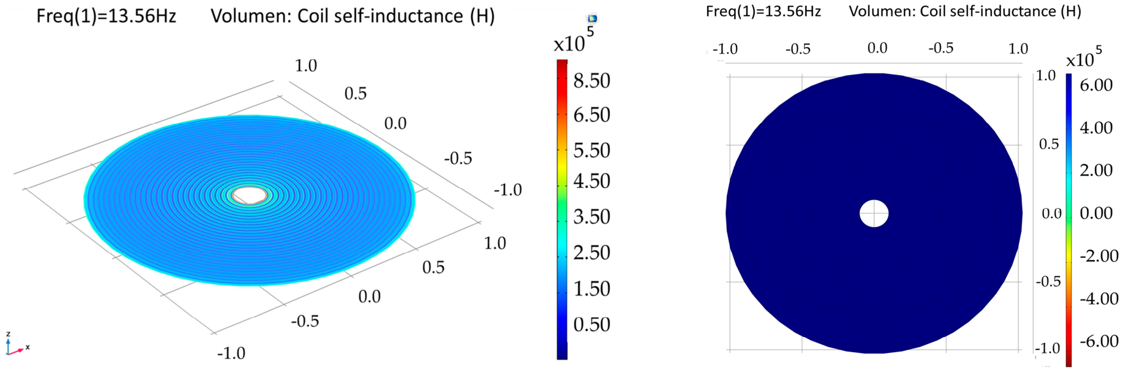

(a) (b)

Figure 14. Simulation results for the internal double-level coil. (a) Self-inductance for the composed double coil and (b) self-inductance for a single-element coil.

The model for a dual-layer planar coil implemented in the implantable set, allows for obtaining higher values of inductance in a small area (restricted by the anatomical dimension of the LV, which results in better characteristics in terms of the internal coupling factor and power transmission efficiency. Table 3 shows the simulation results for the internal coil.

Preprints (www.preprints.org) | NOT PEER-REVIEWED | Posted: 6 July 2018 doi:10.20944/preprints201807.0107.v1

Peer-reviewed version available at *Sensors* **2018**, *18*, 2781; doi:10.3390/s18092781

Table 3. Simulation results for the internal dual coil.

Parameters	Lower loop	Upper loop	Binding
Electrical resistance	77 Ω	158 Ω	259 Ω
Self-inductance	6.68 μH	6.68 μH	21.12 μH
Quality Factor	17	8.3	9.1
Internal coupling factor[1]		0.99	
Internal mutual inductance[1]		6.67 μH	

[1] Parameters between the lower and upper loops.

3.3.2. External coil

The external coil was simulated in a similar way to the internal coil, however, a less complex system was considered, since the coil is formed by a single loop, thus only the explicit simulation model was used. A self-inductance of 19.7 μH, a quality factor of 512 and an electrical resistance of 5.6 Ω were obtained.

3.3.3 Magnetic Coupling link model

The mathematical analysis of the inductive coupling link was validate with the software Comsol Multiphysics based on the near field approximation. The simulation model considers that the external coil is located outside the human body but establishes communication across the surface skin, where the internal coil is mounted within the left ventricle at a depth of 3.5 cm. In addition, we are considering a 13.56 MHz resonance frequency to avoid tissue damage by radiation and heating (according to ISO 14117 for implantable devices), and in order to simulate a more realistic coupling environment, the core considers three types of biological tissue: skin, fat and muscle, as shown in Figure 15. Table 4 shows the parameters used for the composed biological tissue [61-62].

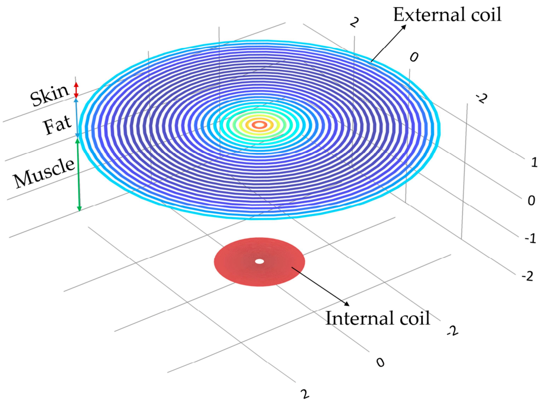

Figure 15. Inductive coupling link across biological tissue.

Table 4. Constitutive parameters of human biological tissue at a frequency of 13.53 MHz.

Model	Thickness [cm]	Conductivity [sm^{-1}]	Relative permittivity	Wavelength [m]
Dry skin	0.5	0.23802	285.25	2.26
Wet skin		0.38421	177.13	2.87
Fat	1	0.030354	11.827	11.11
Muscle	2	0.62818	138.44	3.24

For medical applications, a key factor is the inductive coupling link because part of the field dissipates in the tissue causing some power dissipation. It is clear that as the distance between the

Peer-reviewed version available at *Sensors* **2018**, *18*, 2781; doi:10.3390/s18092781

coils decreases, the electromagnetic field density increases, as well as other parameters such as: the mutual inductance, induced current/voltage and power transmission efficiency. Figure 16 shows the magnetic field density of the inductive coupling link and the relationship between the separation distance between the coils and the induced voltage for an input voltage of 5 V, 10 V and 15 V.

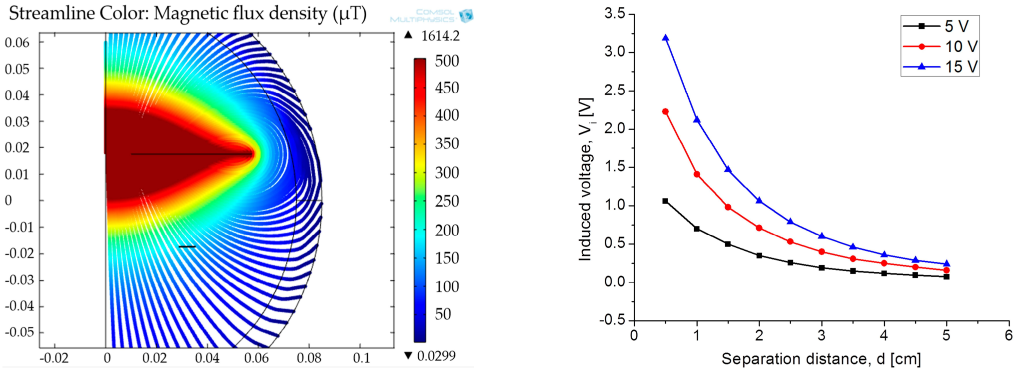

(a) (b)

Figure 16. (a) Magnetic flux density and (b) induced voltage changes as a function of the separation distance.

Finally, the simulation results for the coupling across biological tissue delivers the following results: first, they show a 90% power transmission efficiency under the lower pressure range; second, under the higher pressure range the efficiency decreases to 78%. This controlled coupling attenuation comes from the smooth capacitance transition over the TMCPS array; Figure 17 shows this relationship.

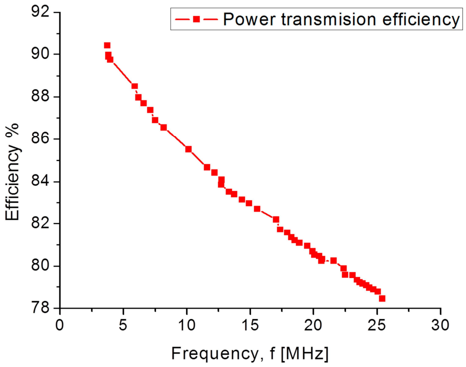

Figure 17. Power transmission efficiency versus frequency.

Table 5 list the simulation parameters about the inductive coupling link, which are in good agreement with the theoretical analysis.

Table 5. Simulation parameters for the inductive coupling link.

Parameters	Symbol	Value
Resonance frequency	f_s	13.56 MHz
Mutual inductance	M	3.38 µH
Magnetic flux density	$\emptyset$	150 µT
Coupling efficiency	k	0.054
Radiation distance	X	3.5 cm
Power transmission efficiency	η	90.7%

5. Conclusions

We report a new sensor scheme offering a continuous blood ventricular pressure monitor, which will allow for the continuous control of some diseases such as heart failure, aortic aneurysms and hypertension. The novel implantable sensor set, composed by capacitive and inductive structures, are arranged over the same flexible substrate, avoiding hybrid-like connections, and combining both manufacturing technologies, surface micromachining and flexible electronics. The capacitive sensors array was designed using a composed aluminum/polyimide diaphragm, where the structure and its parallel interconnection, are arranged in order to cover the wide LV pressure range, which is a key contribution of this work. According to the anatomy of the LV, an internal dual-layer coil was implemented to increase the L and Q parameters in a reduced physical area. The model for a dual-layer planar coil allows for obtaining better characteristics in terms of the internal coupling factor and power transmission efficiency. The implantable set presented the following figures of merit: a dynamic and full 5 mmHg – 300 mmHg pressure range; and an operating frequency range of 5.2–13.56 MHz. This system complies with the full diastolic-systolic pressure range developed across the LV, also following the ISO 14117 standard for implantable devices and the industrial, medical and scientific band (ISM). Currently the fully integrated process fabrication is under progress.

The electromagnetic coupling across the biological tissue was validated with the Comsol Multiphysics software: in the first place showed a 90% power transmission efficiency, at 3.5 cm separation between coils, under the lower pressure range; second, under the higher pressure range the efficiency decreases to 78%. Concerning the module fabrication, and according to our previous experimental work, we adapted the PolyMEMS INAOE® technology, for an aluminum-based technique, which allows for obtaining ergonomic, robust, reproducible, low-cost, and technologically feasible inductive and capacitive structures. The polyimide substrate and coating contribute for reducing the tissue damage and also offers a minimally invasive implantation procedure. Finally, this sensor can also be adapted for monitoring the pressure in different organs such as the aorta, pulmonary artery and the urinary bladder.

Acknowledgments: Natiely Hernandez Sebastián acknowledges Conacyt program scholarship #549792.

Author Contributions: Formal analysis Noe Villa-Villaseñor; Investigation, Natiely Hernández-Sebastián, Daniela Díaz-Alonso and Francisco-Javier Renero-Carrillo, and Wilfrido Calleja-Arriaga. NH Sebastián is a Ph.D. student.

Conflicts of Interest: “The authors declare no conflict of interest."

“The founding sponsors had no role in the design of the study; in the collection, analyses, or interpretation of data; in the writing of the manuscript, and in the decision to publish the results”.

References

1. Yujia, P.; Tengxing, W.; Wein, J.; Xinchuan, L.; Xuejun, W. Modeling and Optimization of Inductively Coupled Wireless Bio-Pressure Sensor System Using the Design of Experiments (DOE) Method. *IEEE Transactions on Components, Packaging and Manufacturing Technology, October 2017, Vol. 8*, pp. 65-72.
2. Guyton, A.C.; Hall J. Textbook of medical physiology. 4th ed., 1032pp. Philadelphia-London-Toronto: Saunders 1971.
3. Collins C. Miniature passive pressure transensors for implanting in the eye. *IEEE Trans Biomed Eng. 1967; Vol. 14*, pp. 74–83.
4. Rosengren, L.; Rangsten, P.; Bäcklund, Y.; Hok, B.; Svedbergh, B.; Selen, G. A system for passive implantable pressure sensors. *Proc. 8th Int. Conf. Solid-State Sensors and Actuators, Yokohama, Japan, 1993*, pp. 588-591.
5. Olsen, E. R. et al. Intracranial pressure measurement with a miniature passive implanted pressure transensor. *Am. J. Surg. 1967, Vol. 113*, pp. 727–729.

6. Wise, K.D.; Clark, S.K. Diaphragm formation and pressure sensitivity in batch-fabricated silicon pressure sensors. *IEDM Tech. Dig., 1978*, pp. 96-99.
7. Lee, Y.S.; Wise, K.D. A batch-fabricated silicon capacitive pressure transducer with low temperature sensitivity. *IEEE Trans. Electron Devices, 1982, vol. ED-29, no. 1*, pp. 42-48.
8. Chatzandroulis, S.; Tsoukalas, D.; Neukomm, P.A. A miniature pressure system with a capacitive sensor and a passive telemetry link for use in implantable applications. *J. Microelectromech. Syst. 2000, vol. 9, no. 1*, pp. 18-23.
9. Park, E.C.; Yoon, J.B.; Yoon, E. Hermetically sealed inductor–capacitor (LC) resonator for remote pressure monitoring. *Jpn. J. Appl. Phys. 1998, Vol. 37*, pp. 7124-7128.
10. Takahata, K.; DeHennis, A.; Wise K.D.; Gianchandani Y.B. A wireless microsensor for monitoring flow and pressure in a blood vessel utilizing a dual-inductor antenna stent and two pressure sensors. *Int. Conf. Micro Electro Mechanical Systems, 2004, Vol. 17*, pp. 216-9.
11. DeHennis, A.; Wise, K.D. A fully-integrated multisite pressure sensor for wireless arterial flow characterization. *Dig. North American Sensor Actuator Microsystems Workshop, 2004, Vol. 15*, pp. 168-171.
12. Información General sobre Hipertensión en el Mundo. Available online. http://apps.who.int/iris/bitstream/handle/10665/87679/WHO_DCO_WHD_2013.2_spa.pdf;jsessionid=CA28E7F834B1972192D25482E211BCBC?sequence=1 (Accessed on 15 March 2018).
13. Banegas, J.R.; Ruilope, L.M. Mortality study from the Spanish Registry of ABPM. An appeal for the transition of ABPM to clinical practice. *Hipertensión y riesgo cardiovascular, September 2018*, pp.97-100.
14. Campos, C.N.; Lucia, H.C. Hipertensión en adultos mexicanos: prevalencia, diagnóstico y tipo de tratamiento. Salud pública de México, vol. 6, mayo 2018.
15. Maria, T.L. Burden of hypertension as a cardiovascular risk factor. *Revista médica clínica los condes, Marzo 2015, Vol. 26*, pp. 156-163.
16. Lanzarini, L.; Fontana, A.; Campana, C.; Klersy, C. Two simple echo-Doppler measurements can accurately identify pulmonary hypertension in the large majority of patients with chronic heart failure. *J Heart Lung Transplant. 2005, Vol. 24*, pp. 745–754.
17. Hugo, E.V.; Pablo, F.C.; Roberto, A.F.; Mario, A.A.; Milton, E.A.; Carlos, C.D.; Robert, C.B. Comparison of a Radiofrequency-Based Wireless Pressure Sensor to Swan-Ganz Catheter and Echocardiography for Ambulatory Assessment of Pulmonary Artery Pressure in Heart Failure. *Journal of the American College of Cardiology. Dec 2007, Vol. 50 (25)*, pp. 2375-2382; DOI: 10.1016/j.jacc.2007.06.061.
18. Ogedegbe, G.; Pickering, T. Principles and Techniques of Blood Pressure Measurement. *Cardiology Clinics, 2010, Vol. 28*, pp.571-586.
19. Fonarow, G.C.; Stevenson, L.W.; Walden, J.A.; et al. Impact of comprehensive heart failure management program on hospital readmission and functional status of patients with advanced heart failure. *J Am Coll Cardiol, 1997, Vol. 30*, pp. 725–732.
20. Fonarow, G.C.; Chelimsky-Fallik, C.; Stevenson, L.W.; et al. Effect of direct vasodilation with hydralazine versus angiotensin-converting enzyme inhibition with captopril on mortality in advanced heart failure: *The HyC trial. J Am Coll Cardiol. 1992, Vol. 19*, pp. 842–850.
21. Stevenson, L.W.; Tillish, T.H. Maintenance of cardiac output with normal filling pressures in patients with dilated heart failure. *1986, Vol. 74*, pp. 1303–1308
22. Fonseca, M.A.; Allen, M.G.; Kroh, J.; White, J. Flexible wireless passive pressure sensors for biomedical applications. *Proc. 12th Solid-State Sens. Actuators Microsyst. Workshop, 2006*, pp. 37-42.
23. CardioMEMS™. Available online. https://www.accessdata.fda.gov/cdrh_docs/pdf10/p100045c.pdf (Accessed on 21 February 2018).
24. Clausen, I.; Glott, T. Development of Clinically Relevant Implantable Pressure Sensors: *Perspectives and Challenges. Sensors, 2014*, pp. 17686–17702.
25. CardioMEMS, CardioMEMS, inc. announces FDA clearance of the EndoSureä wireless AAA pressure measurement system for measuring intrasac pressure during thoracic aortic aneurysm (TAA) repair. Available Online. http://www.cardiomems.com/content.asp?display=news&view=9 (Accessed on 21 on February 2018).
26. Host, J.F.; Hasan A. Role of telephone monitoring in patients with chronic heart failure: theory and practical implications. *Smart Homecare Technology and TeleHealth, 2014*, pp. 1–12.

Peer-reviewed version available at *Sensors* **2018**, *18*, 2781; doi:10.3390/s18092781

27. Pandey, A.C. et al. Reducing Days in the Hospital with Cardiomems Device in Patients with Left Ventricular Assist Device. *The Journal of Heart and Lung Transplantation, Vol. 37, Issue 4*, pp. S280 - S281.
28. Rodrigo, B. Revolucionando el tratameinto de la insuficiencia cardíaca descubriendo CardioMEMSTM: Descubriendo CardoMEMST. *Insuficiencia cardíaca, 2015, Vol. 10(3),* pp. 141-148.
29. Abraham, W.T.; Stevenson, L.W.; Bourge, R.C.; Lindenfeld, J.A.; Bauman J.G.; Adamson, P.B. CHAMPION Trial Study Group. Sustained efficacy of pulmonary artery pressure to guide adjustment of chronic heart failure therapy: complete follow-up results from the CHAMPION randomised trial. *Lancet, 2016, Vol. 387*, pp. 453–461. DOI: 10.1016/S0140-6736(15)00723-0.
30. Ahmed, D. RVSP – Right Ventricular Systolic Pressure: MyHeart. Available online. https://myheart.net/articles/rvsp-right-ventricular-systolic-pressure/ (Accessed on February 2018).
31. Takahata, K.; DeHennis, A.; Wise, K.D.; Gianchandani, Y.B. A micromachined antenna stent for wireless monitoring of implantable microsensors. *Proc. Annu. Int. Conf. IEEE Eng. Med. Biol. Soc. 4, 2004, pp.* 3360–3363.
32. DeHennis, A.D.; Wise, K.D. A fully integrated multisite pressure sensor for wireless arterial flow characterization. *J. Microelectromech. Syst. 15, 2006*, pp. 678–685.
33. CardioMEMS. Available Online. http://www.cardiomems.com (Accessed in 2018).
34. Allen, M.G. Micromachined endovascularly-implantable wireless aneurysm pressure sensors: from concept to clinic Transducers, *2005*, pp. 275–278.
35. Hamilton, M.A.; Stevenson, L.W.; Child, J.S.: Moriguchi, J.D.; Walden, J.; Woo, M. Sustained reduction in valvular regurgitation and atrial volumes with tailored vasodilator therapy in advanced congestive heart failure secondary to dilated (ischemic or idiopathic) cardiomyopathy. *Am J Cardiol, 1991, Vol. 67,* pp. 259–263.
36. Harvey, S.; Stevens, K.; Harrison, D.; et al. An evaluation of the clinical and cost-effectiveness of pulmonary artery catheters in patient management in intensive care: a systematic review and a randomized controlled trial. *Health Technol. 2006, Vol. 10,* pp. 1–150.
37. Merchant, F.M.; Dec, G.W.; Singh, J.P. Implantable sensors for heart failure. *Circ Arrhythm Electrophysiol. 2010, Vol. 3,* pp. 657-667.
38. Adamson, P.B.; Magalski, A; Braunschweig, F.; Bohm, M.; Reynolds, D.; Steinhaus, D.; Luby, A.; Linde, C.; Ryden, L.; Cremers, B.; Takle, T.; Bennett, T. Ongoing right ventricular hemodynamics in heart failure: clinical value of measurements derived from an implantable monitoring system. *J Am Coll Cardiol. 2003, Vol. 41,* pp. 565–571.
39. Magalski, A.; Adamson, P.; Gadler, F.; Boehm, M.; Steinhaus, D,; Reynolds, D.; Vlach, K.; Linde, C.; Cremers, B.; Sparks, B.; Bennett, T. Continuous ambulatory right heart pressure measurements with an implantable hemodynamic monitor: a multicenter, 12-month follow-up study of patients with chronic heart failure. *J Card Fail. 2002, Vol. 8*, pp. 63–70.
40. Adamson, P.B.; Kjellstrom, B.; Braunschweig, F.; Magalski, A.; Linde, C.; Kolodiezj, A.; Cremers, B.; Bennett, T. Ambulatory hemodynamic monitoring from an implanted device: components of continuous 24-hour pressures that correlate to supine resting conditions and acute right heart catheterization. *Congest Heart Fail. 2006, Vol. 12,* pp. 14–19.
41. Thomas, M.; Philip B.; Jason, W.; Jin W.P.; Jessic,a H.; Julia, V.; Peter K.; Stuart, W.; Peter, S.; Erwin, B.; Wilfried, D.; Jörg H.; Hubert T. Remote Left Ventricular Hemodynamic Monitoring Using a Novel Intracardiac Sensor. *Journal of the American College of Cardiology.*
42. Mosterd, A.; Azadas, A.W. Epidemiología clínica de la insuficiencia cardíaca. *Heart. 2007 , Vol. 93,* pp. 1137 – 1146. Doi: 10.1136 / hrt.2003.025270.
43. Zile, M.R.; Bennett, T.D.; John, S.M.; Cho, Y.K.; Adamson, P.B.; Aaron, M.F.; Aranda, J.M.; Braham, W.T.; Smart, F.W.; Stevenson, L.W.; Kueffer, F.J.; Bourge, R.C. Transición de la insuficiencia cardíaca crónica compensada a la descompensada aguda: información fisiopatológica obtenida de la monitorización continua de las presiones intracardíacas. *2008, Vol. 118,* pp. 1433 – 1441. Doi: 10.1161 / CIRCULATIONAHA.108.783910.
44. Roberto M.L; Luigi P.B.; Víctor, M.; Jonathan, A.. Recomendaciones para la Cuantificación de las Cavidades Cardiacas por Ecografía en Adultos: Actualización de la Sociedad Americana de Ecocardiografía y de la Asociación Europea de Imagen Cardiovascular. *Chicago Illinois; Padua, Italia, Quebec y Toronto. American Society of Echocardiography. 2015.*

45. Rendón-Nava, A.; Díaz-Méndez, J.; Nino-de-Rivera, L.; Calleja-Arriaga, W.; Gil-Carrasco, F.; Díaz-Alonso, D. Study of the Effect of Distance and Misalignment between Magnetically Coupled Coils for Wireless Power Transfer in Intraocular Pressure Measurement. *The Scientific World Journal, 2014,* pp.1-11.
46. Díaz, D. Caracterización y modelado de sensores capacitivos para aplicaciones médicas. PhD. *Instituto Nacional de Astrofísica, Óptica y Electrónica. 2015.*
47. Díaz, D.; Mario, M.M., Carlos, Z.; Joel, M.; Wilfrido-Calleja, A.; Juan- Carlos, C., Luis-Niño, R.; Volodymir, P.; Felix, G.; Angel, G.; Efrain, R. Hermetic capacitive pressure sensors for biomedical applications. *Microelectronics International, 216, Vol. 33 Issue: 2,* pp.79-86,
48. Carrasco, F.; Alonso, D.; Niño-de-Rivera, L. Biocompatibility and implant of a less invasive intraocular pressure sensor. *Microelectronic Engineering, 2016, Vol. 159,* pp.32-37.
49. Chen, P.J.; Saati, S.; Varma, S.; Humayun, M.S.; Tai, Y.C. Wireless intraocular pressure sensing using microfabricated minimally invasive flexible-coiled LC sensor implant. *J. Microelectromechan. Syst., 2010, vol. 19, no. 4,* pp. 721-734.
50. Chen, P.J.; Rodger, D.; Saati, S.; Humayun, M.S.; Tai, Y.C. Microfabricated Implantable Parylene-Based Wireless Passive Intraocular Pressure Sensors. Journal of Microelectromechanical Systems, 2018, 17(6), pp.1342-1351.
51. Hannan, M. A.; Mutashar, S.; Samad, S. A.; Hussain, A. Energy harvesting for the implantable biomedical devices: issues and challenges. Biomed. Eng. Online 13, 2014, pp. 79.
52. Finkenzeller, K. RFID Handbook: Fundamentals and Applications in Contactless Smart Cards and Identification, 2nd ed.; Wiley: New York, NY, USA, 2003.
53. Ko, W.H.; Wang, Q. Touch mode capacitive pressure sensors. *Sensors and Actuators, 1999, vol. A 75,* pp. 242-251.
54. Yamamoto, S.; Nakao, O.; Nishimura, H. Touch mode capacitive pressure sensor for passive tire monitoring system. *Proc. Sensors of IEEE, 2002, vol 2,* pp 1582-6.
55. Timoshenko, S.P.; Woinowsky, K.S. Theory of Plates and Shells. Second Edition, Mc-Graw-Hill Book, 1959, New York, NY.
56. Islam, A.; Islam, S. Design of multi-spiral solenoidal inductor for inductive power transfer in biomedical applications. *Proc. Applied Computational Electromagnetics Society Conf., 2011,* pp. 369-374.
57. Zhao J. A new calculation for designing multilayer planar spiral inductors. *EDN, July 2010, vol. 29,* pp. 37-40.
58. Chiang, C.; Klin, C.; Ju, M. An implantable capacitive pressure sensor for biomedical applications. *Sens. Actuators, A, 2007, Vol. 134,* pp. 382-388.
59. Mutashar, S.; Hannan, M.A.; Samad, S.A.; Hussain, A. Analysis and optimization of spiral circular inductive coupling link for bio-implanted applications on air and within human tissue. *Sensors, Vol. 14,* pp. 11522-11541, 2014.
60. Mutashar, S.; Hannan, M.A.; Samad, S.A.; Hussain, A. Efficiency Improvement of Wireless Power Transmission for Bio-Implanted Devices. *International Journal of Medical, Health, Biomedical, Bioengineering and Pharmaceutical Engineering. 2013, Vol:7, No:12.*
61. Hmida, G.B.; Ghariani, H.; Samet, M. Design of wireless power and data transmission circuits for implantable biomicrosystem. Biotechnol. *J. 2007, vol. 6, no. 2,* pp. 153-164, 2007.
62. Rahko, P.S. Evaluation of the skin-to-heart distance in the standing adult by two-dimensional echocardiography. *J Am Soc Echocardiogr, Jun 2008, Vol. 21(6),* pp. 761-764.